

# Enhanced Thermoelectric Performance in Ternary Skutterudite $\text{Co}(\text{Ge}_{0.5}\text{Te}_{0.5})_3$ via Band Engineering

Suneesh Meledath Valiyaveetil, Duc-Long Nguyen, Deniz P. Wong, Cheng-Rong Hsing, Laura Paradis-Fortin, Mohammad Qorbani, Amr Sabbah, Ta-Lei Chou, Kuei-Kuan Wu, Vasudevan Rathinam, Ching-Ming Wei\*, Li-Chyong Chen\*, Kuei-Hsien Chen\*

**KEYWORDS:** skutterudite, thermoelectrics, band engineering, multiband effect, phonon scattering

---

**ABSTRACT:** We report the phase evolution and thermoelectric properties of a series of  $\text{Co}(\text{Ge}_{0.5}\text{Te}_{0.5})_{3-x}\text{Sb}_x$  ( $x = 0-0.20$ ) compositions synthesized by mechanical alloying. Pristine ternary  $\text{Co}(\text{Ge}_{0.5}\text{Te}_{0.5})_3$  skutterudite crystallizes in the rhombohedral symmetry ( $R\bar{3}$ ), and Sb doping induces a structural transition to the cubic phase (ideal skutterudite,  $Im\bar{3}$ ). The Sb substitution increases the carrier concentration while maintaining a high thermopower even at higher doping levels, owing to an increased effective mass. The exceptional electronic properties exhibited by  $\text{Co}(\text{Ge}_{0.5}\text{Te}_{0.5})_3$  upon doping are attributed to the carrier transport from both the primary and secondary conduction bands, as shown by theoretical calculations. The enhanced electrical conductivity and high thermopower increase the power factor by more than 20 times. Because the dominant phonon propagation modes in binary skutterudites are associated with the vibrations of pnictogen rings, twisting the latter through the isoelectronic replacement of  $\text{Sb}_4$  rings with  $\text{Ge}_2\text{Te}_2$  ones, as done in this study, can effectively reduce the thermal conductivity. This leads to an increase in the dimensionless figure-of-merit ( $zT$ ) by a factor of 30, reaching 0.65 at 723 K for  $\text{Co}(\text{Ge}_{0.5}\text{Te}_{0.5})_{2.9}\text{Sb}_{0.1}$ .

---

## 1. INTRODUCTION

In the realm of technologies to increase energy efficiency, thermoelectric materials, that convert thermal and electrical energy through solid-state phenomena, has captivated a lot of interest from the scientific community. Thermoelectric power generation, involving the conversion of waste heat to electricity via the Seebeck effect in serial  $p$ - $n$  semiconductor pairs, is considered among the best alternatives to fossil energies.<sup>1-6</sup> However, a large improvement in conversion efficiency is required for most materials, which is a major challenge because of the strong correlation between their electrical and thermal properties.

The skutterudite materials are a class of “phonon glass electron crystals” with chemical formula  $\text{MX}_3$ , where M is a group IX (Co, Rh, or Ir) transition metal and X is a group XV (P, As, or Sb) pnictogen, which crystallizes in a cubic structure with large voids and four-membered rings of X atoms.<sup>7, 8</sup> Among skutterudite materials, heavily doped  $n$ -type  $\text{CoSb}_3$  exhibits favorable electronic transport features, originating from the presence of a multivalley secondary conduction band (CB).<sup>9</sup> As the temperature increases, the energy difference between conduction band minimum (CBM) and second CB edge decreases, eventually leading to band convergence at elevated temperature with carrier transport occurring in both bands, resulting in a higher thermopower ( $S$ ).<sup>9-12</sup> Apart from exhibiting favorable intrinsic electronic

properties, the most unique feature of skutterudite materials is their capability to fill the large void spaces in their crystal structure with rattlers,<sup>13, 14</sup> which can achieve the dual purpose of improving the power factor by electron doping<sup>15</sup> and reducing the lattice thermal conductivity via the rattling effect.<sup>16, 17</sup> Apart from rattling effect, nanostructuring is an effective way to reduce lattice thermal conductivity in skutterudite materials.<sup>18-20</sup> An alternative way to reduce the lattice thermal conductivity is to distort the rectangular pnictogen rings, because the vibrations of the latter dominate the phonon spectrum of binary skutterudites.<sup>21, 22</sup> One way to disrupt the pnictogen ring is the isoelectronic substitution of the pnictogen (group V) element by group IV-VI pairs, thus keeping the valence electron count per unit cell unchanged to 144  $e^-$  and the whole system in a diamagnetic semiconducting state.<sup>23, 24</sup> Hence, our recent efforts were focused on the synthesis and characterization of ternary skutterudites, with the same electron count per unit cell as their binary counterparts. Previous crystallographic studies of the resulting ternary skutterudites revealed a distortion of the nearly square pnictogen ring, with the anion atoms exhibiting long-range ordering. In practice, the group IV and VI elements are not distributed randomly, but reside at the opposite corners of the four-membered rings, along the  $[111]$  direction.<sup>25-28</sup> The distortion of the four-membered rings, leading to a symmetry reduction from cubic ( $Im\bar{3}$ ) to rhombohedral ( $R\bar{3}$ ), was mainly attributed to the stronger interactions between

the transition metals and the group IV (Ge) than group VI (Te) anions.<sup>29</sup>

To date, most experimental and theoretical studies on ternary skutterudites have focused on undoped pristine compositions. These studies reported higher Seebeck coefficient and electrical resistivity values for the ternary materials compared to their binary counterparts, while their more complex unit cell resulted in lower thermal conductivity.<sup>25-27, 30-33</sup> Although achieving a low thermal conductivity is essential to improve the dimensionless figure-of-merit ( $zT$ ) value, modifying the electronic structure and thus the electronic transport efficiency is the key challenge in the case of ternary skutterudite  $\text{Co}(\text{Ge}_{0.5}\text{Te}_{0.5})_3$ . Tight-binding band structure (BS) calculations showed that the nature of the electronic bands near the Fermi level is mostly governed by the presence of the  $X_4$  planar rings.<sup>29</sup> Moreover, previous theoretical studies showed that the electronic band structure of ternary skutterudites can be radically altered by modifying the structure of the anion rings.<sup>34</sup> Nevertheless, the extrinsic doping of  $\text{Co}(\text{Ge}_{0.5}\text{Te}_{0.5})_3$  has never been reported to date.

This work paves the way to a better understanding of the influence of electron (Sb) doping on the crystal structure and thermoelectric properties of charge-compensated ternary skutterudite. We also report the band structures of the  $\text{Co}(\text{Ge}_{0.5}\text{Te}_{0.5})_3$  and examine its correlation with that of the binary counterpart,  $\text{CoSb}_3$ . To determine the crystallographic occupancy of Sb in  $\text{Co}(\text{Ge}_{0.5}\text{Te}_{0.5})_3$ , we first investigated the formation energy of the Sb substitution process and calculated the band structure of all possible configurations. Experimentally, it was observed that, as the Sb doping increases, the electrical conductivity ( $\sigma$ ) is substantially enhanced while the  $n$ -type thermopower remains high, as a result of the increased effective mass. A similar behavior is observed in  $\text{CoSb}_3$ , where the multivalley secondary bands concept has been used to explain the increase in effective mass. The fundamental question is whether the explanation based on the multi-band effect is also valid for the charge-compensated ternary skutterudites. To answer this question, we theoretically demonstrated the increasing trend of the effective mass with different Sb concentrations and further calculated the thermopower at different carrier concentrations. In addition, the lattice thermal conductivity of ternary skutterudite  $\text{Co}(\text{Ge}_{0.5}\text{Te}_{0.5})_3$  was significantly lower compared to that of its binary counterparts. To probe the physical influence of the pnictogen ring configuration on the lattice thermal conductivity, we investigated the lattice dynamics in both binary and ternary skutterudite material systems.

## 2. EXPERIMENTAL SECTION

### 2.1. Sample Preparation and Characterizations

The skutterudite-type  $\text{Co}(\text{Ge}_{0.5}\text{Te}_{0.5})_{3-x}\text{Sb}_x$  compounds were prepared by mixing stoichiometric amounts of high-

purity Co, Ge, Te, and Sb elemental powders (all > 99.99%, obtained from Sigma-Aldrich) via a mechanical alloying process; for the latter, we employed a planetary ball mill (Retsch PM100) operating at RT, at a disc rotation speed of 300 rpm for 10 h. Working inside an Ar-filled glove box, the chemicals were weighed and loaded into a stainless steel jar with tungsten carbide balls, with a powder-to-ball weight ratio of 1:20. The as-milled powders were then placed into a graphite molding die and consolidated by hot-pressing at 873 K for 30 min under a 50 MPa pressure. The resulting pellets had a diameter of 15 mm, a thickness of 2.5 mm, and geometrical densities greater than 97%. The synthesis and sintering conditions were optimized to yield the sample with highest purity.

After finely grinding the products, the sample purity and nature were checked by X-ray powder diffraction with a two-circle diffractometer (D2 Phaser, Bruker,  $\theta$ - $2\theta$  Bragg-Brentano mode) equipped with a Cu X-ray tube and a LynxEye XE-T detector. The best samples were selected for high-resolution synchrotron XRD measurements, which were carried out on the TPS BL 19A beamline of the National Synchrotron Radiation Research Center (NSRRC), Taiwan. Diffractograms were recorded on skutterudite  $\text{Co}(\text{Ge}_{0.5}\text{Te}_{0.5})_{3-x}\text{Sb}_x$  powders in borosilicate capillaries ( $\Phi_{\text{external}} = 0.1$  mm) on a 9-circle diffractometer at 15 KeV ( $\lambda = 0.8265$  Å). The patterns were collected by a multicrystal analyzer detector mounted on a goniometer head, over a  $2\theta$  range of  $2$ – $100^\circ$  with a step size of  $\sim 0.004^\circ$ . Pattern refinement was carried out with the Le Bail method using the Winplotr and Fullprof software packages.<sup>35-36</sup> The shape of the diffraction peaks was approximated using a Thompson-Cox-Hastings pseudo-Voigt function.<sup>37</sup> The zero-point shift and shape parameters were systematically refined, and the background contribution was estimated manually. Finally, we refined the lattice and isotropic displacement parameters (*i.e.*, Debye-Waller factors,  $B_{\text{ISO}}$ ). High-resolution transmission electron microscopy (HRTEM, JEOL-2100, 200 kV) was used to record the microstructures and selected-area electron diffraction (SAED) patterns of the samples.

To investigate the electrical properties, including  $\sigma$ ,  $S$ , and the corresponding thermoelectric power factor  $S^2\sigma$ , a rectangular ingot ( $\sim 3$  mm  $\times$  3 mm  $\times$  15 mm) was cut from a hot-pressed pellet and analyzed with a ULVAC-RIKO ZEM-3 system under helium atmosphere from RT to 773 K. In the same temperature range, a NETZSCH LFA-457 apparatus was used to measure the thermal diffusivity under argon flow. The thermal conductivity was determined as the product of thermal diffusivity, density (obtained by the Archimedes method), and heat capacity (estimated by the Dulong-Petit approximation). To calculate the lattice thermal conductivity by subtracting the electronic contribution from the total thermal conductivity ( $\kappa_L = \kappa - \kappa_e$ ), we used the Wiedemann-Franz law with a Seebeck-dependent Lorenz number. The estimated measurement uncertainties were 6% for the Seebeck coefficient, 8% for the electrical resistivity, 11% for the thermal conductivity, and

16% for the figure-of-merit.<sup>38</sup> Room-temperature Hall effect measurements were carried out using a HMS-3000 system in Van-der Pauw configuration with a 0.55 T magnetic field, which is further confirmed by using Quantum Design Physical Property Measurement System (PPMS) with 3T magnetic field. Carrier concentrations were calculated by assuming a single parabolic band conduction model, using the formula  $n = 1/R_H e$ , where  $e$  is the electronic charge.

## 2.2. DFT Calculations

First-principles total energy calculations based on DFT were performed with the Vienna ab initio simulation package,<sup>39</sup> using the projector augmented-wave method<sup>40, 41</sup> and plane-wave basis sets. The valence electron configurations of adopted pseudopotentials for Co, Ge, Te, and Sb atoms are 9 ( $d^8s^1$ ), 4 ( $s^2p^2$ ), 6 ( $s^2p^4$ ), and 5 ( $s^2p^3$ ), respectively. We used a hexagonal unit cell with  $a = 12.408 \text{ \AA}$  and  $c = 15.197 \text{ \AA}$ , containing 24 Co, 36 Ge, and 36 Te atoms; Sb atoms were then substituted for Ge or Te atoms to obtain the optimized lowest-energy structures. Brillouin zone summation was performed with a  $3 \times 3 \times 3$  k-point grid. The plane-wave energy cutoff was set to 400 eV. Self-consistent total energy calculations were carried out until the energy was converged to 0.001 meV/cell, and atomic positions were relaxed until the residual forces were less than 5 meV/Å. The energy and force convergences were carefully checked. We employed the generalized gradient approximation (GGA)<sup>42</sup> with the Perdew–Burke–Ernzerhof (PBE) parametrization.<sup>43</sup>

The calculation of phonon dispersions and lattice thermal conductivities requires information on the second-order and third-order interatomic force constants (IFCs). To obtain these data, we used the HIPHIVE package,<sup>44</sup> which is interfaced with machine-learning libraries providing efficient implementations of linear regression and direct enumeration approaches for the extraction of IFCs of different orders. To obtain the reference data, we used the Monte Carlo rattle approach<sup>44</sup> to generate 25 structures based on a  $2 \times 2 \times 2$  (256 atoms) supercell of the conventional  $\text{CoSb}_3$  (32 atoms) and  $\text{Co}(\text{Ge}_{0.5}\text{Te}_{0.5})_3$  (32 atoms) cells, with an average displacement amplitude of 0.08 Å. Forces acting on the atoms of these generated structures were calculated using DFT, with similar parameters to those used in the electronic structure calculations. The underlying force constant potentials (FCP) were reconstructed using the recursive feature elimination (RFE) feature selection method. The FCPs were then used in combination with the Phonopy package<sup>45</sup> to analyze the material thermal properties in the harmonic approximation, while third-order force constants such as phonon lifetimes (considering only phonon-phonon scattering) were analyzed using the Phono3py package.<sup>46</sup>

## 3. RESULTS AND DISCUSSION

### 3.1. Structural Characterization

In the following, we show that two types of compounds can be synthesized in the  $\text{Co}(\text{Ge}_{0.5}\text{Te}_{0.5})_{3-x}\text{Sb}_x$  system: an ordered ( $x = 0$ ) and an ideal ( $x = 0.15$  and  $0.20$ ) skutterudite structure, as well as a solid solution of the two ( $x = 0.05$  and  $0.10$ ).

The synchrotron X-ray powder diffraction (SXPRD) patterns of the  $\text{Co}(\text{Ge}_{0.5}\text{Te}_{0.5})_{3-x}\text{Sb}_x$  ( $x = 0-0.20$ ) samples are displayed in Figure 1a. The relative percentages of secondary phases were determined by Rietveld refinement. The pristine sample was refined using the rhombohedral structural model (Figure S1, and summarized the parameters in Table S1) and the  $x = 0.10$  sample by distributing the Sb atoms on the anionic sites based on DFT results (Figure S2, and the parameters summarized in Table S3). A careful examination of the diffraction data of the five samples showed that all prepared materials contained  $\sim 6\%$  of binary tellurides ( $\text{CoTe}_2$ , indicated by exclamation point symbols in Figure 1a), and  $\sim 1\%$  of binary oxides ( $\text{GeO}_2$ , star symbols in Figure 1a) (Table S3); these amounts are comparable to those reported in literature for similar materials.<sup>28</sup> The addition of Sb ( $x = 0.10, 0.15, \text{ and } 0.20$ ) promoted the formation of GeTe as secondary phase (hash symbols in Figure 1a), as a consequence of the replacement of Ge-Te by Sb-Sb pairs in the anion rings. In addition, a peak shift toward higher angles was observed for the  $\text{CoTe}_2$  phase (Figure 1b), as a result of the decrease in lattice parameters due to some of the Sb atoms entering the secondary phase. Consequently, the precise amount of Sb entering the main phase is unknown, but the stoichiometry obtained from electron probe microanalysis (EPMA) measurements (Table S4) is a good approximation, as  $\text{CoTe}_2$  represents only 6 wt.% of the sample.

The XRD patterns of all five samples could be indexed to a cubic ( $Im\bar{3}$ ) lattice. However, the powder diffraction patterns of the  $x = 0, 0.05, \text{ and } 0.10$  samples showed weak reflections ( $\sim 16.4^\circ$ , Figure 1b), violating the body-centering condition ( $h + k + l = 2n$ ) of the ideal skutterudite structure. These additional reflections could be indexed using the ordered skutterudite ( $R\bar{3}$ ) structure reported previously.<sup>27, 28, 47</sup> The space group and corresponding lattice parameters obtained for the pristine sample were  $R\bar{3}$  and  $a = 12.3193(2)\text{ \AA}$ ,  $c = 15.0972(2)\text{ \AA}$ , respectively, whereas those of the end member of the series [ $\text{Co}(\text{Ge}_{0.5}\text{Te}_{0.5})_{2.8}\text{Sb}_{0.20}$ ] were  $Im\bar{3}$  and  $a = 8.7344(1)\text{ \AA}$ . The FWHM of these additional reflections ( $\sim 0.09^\circ$ ) was substantially larger than that of the intense reflections ( $\sim 0.04^\circ$ ). This anisotropic broadening of the powder X-ray diffraction peaks can be attributed to anionic disorder. Hence, Rietveld refinements with both ideal ( $Im\bar{3}$ ,  $R_{\text{Bragg}} = 8.82$ ) and ordered [space group  $R\bar{3}$ ,  $R_{\text{Bragg}} = 3.61$ ,  $R_{\text{Bragg}} = 3.41$  (anisotropic)] skutterudite models were performed on the pristine sample (Figure S1). The refinements in the  $R\bar{3}$  group did not result in significantly better agreement between observed and calculated data, regardless of the larger number of refined parameters and the addition of anisotropic broadening parameters.

The shift of the diffraction peaks toward lower angles with increasing Sb substitution indicates an increase of the

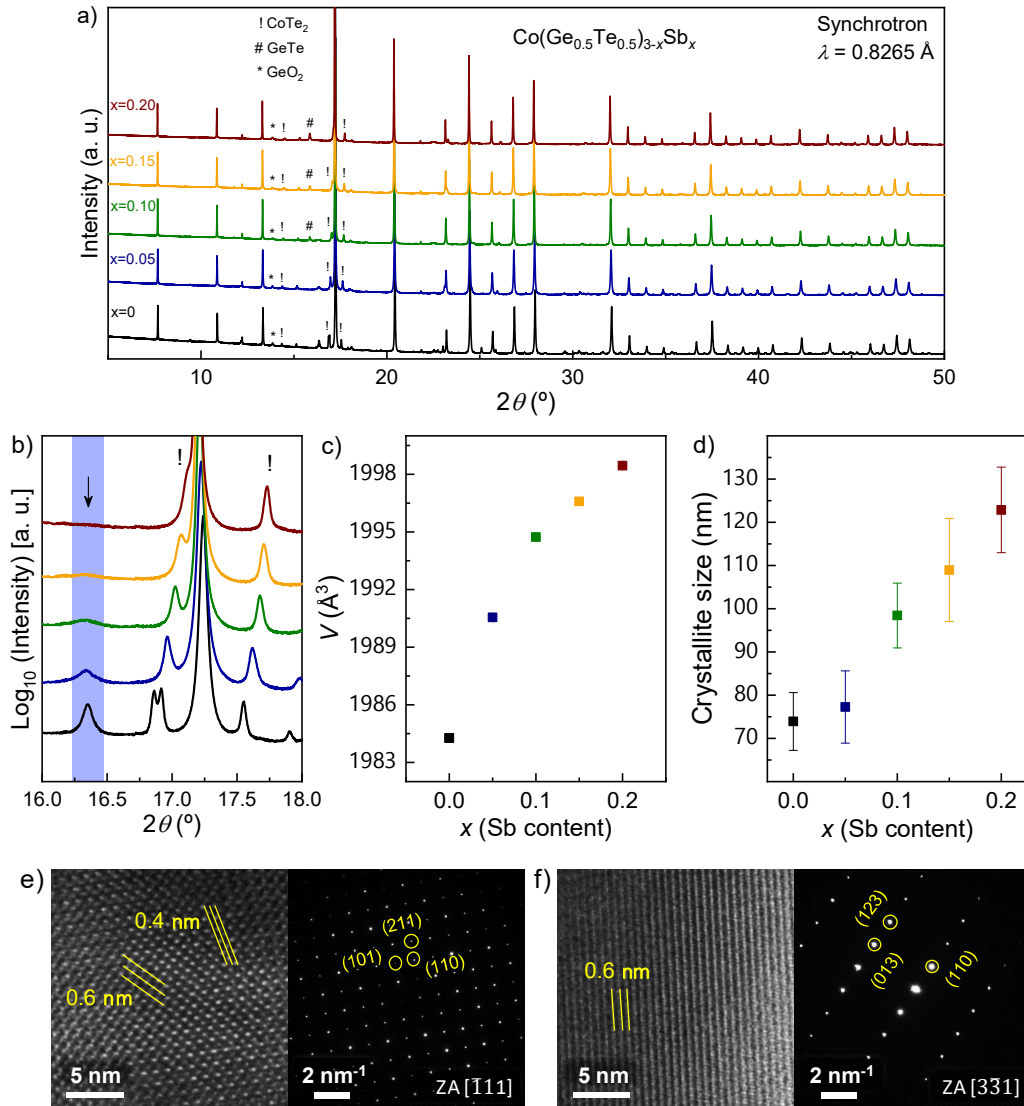


**Figure 1.** (a) Synchrotron XRD data for  $\text{Co}(\text{Ge}_{0.5}\text{Te}_{0.5})_{3-x}\text{Sb}_x$  ( $x = 0-0.20$ ) compounds. (b) Logarithmic plot of XRD data showing the peak shift and phase transition (blue highlight and arrow symbol) occurring in the system. (c, d) Variation of lattice parameter (c) and crystallite size (d) with Sb concentration for  $\text{Co}(\text{Ge}_{0.5}\text{Te}_{0.5})_{3-x}\text{Sb}_x$  ( $x = 0-0.20$ ) compounds. (e, f) HRTEM images (left panels) and SAED patterns (right panels) of (e) pristine  $\text{Co}(\text{Ge}_{0.5}\text{Te}_{0.5})_3$  and (f)  $\text{Co}(\text{Ge}_{0.5}\text{Te}_{0.5})_{2.8}\text{Sb}_{0.20}$  samples. ZA stands for zone axis.

lattice parameters in the series (Figures 1a and 1b). For the purpose of comparing the lattice parameters, all samples were refined by the Le Bail method in the  $R\bar{3}$  space group. The lattice parameters, shown as lattice volume, of each sample are plotted as a function of the Sb content in Figure 1c.

Based on Vegard's law, according to the highly linear trend for the Sb compositions with  $x = 0.05-0.20$ , we can conclude that the dopant was successfully incorporated in the skutterudite structure. Using tight-binding calcula-

tions, a previous study showed that  $d\pi-p\pi$  bonding between Ge and Co atoms is responsible for the diamond-shape distortion of  $\text{Ge}_2\text{Q}_2$  rings in  $\text{Co}(\text{Ge}_{0.5}\text{Q}_{0.5})_3$  ( $\text{Q} = \text{S}, \text{Se}$ ).<sup>48</sup> This is consistent with the trends observed here: the  $\text{Ge}_2\text{Te}_2$  geometry shifted toward the cubic geometry of the ideal skutterudite structure with increasing size of anions. The transition from hexagonal to cubic symmetry induced by the Sb substitution is beyond the scope of this study and is currently being investigated using resonant diffraction. The crystallite size estimated using the Scherrer equation

was  $\sim 80$  nm and increased with increasing Sb content (Figure 1d). The scanning electron microscope (SEM) images of the samples  $\text{Co}(\text{Ge}_{0.5}\text{Te}_{0.5})_{3-x}\text{Sb}_x$  ( $x = 0$  and  $0.10$ ) shows the uniform distribution of the grains (Figure S3). Figure 1e (left panel) shows  $d$ -spacing values of  $0.62 \pm 0.03$  and  $0.41 \pm 0.02$  nm assigned to the  $(110)$ , and  $(211)$  planes, respectively. Selected-area electron diffraction (SAED) patterns shows the pristine sample has a lattice with  $R\bar{3}$  symmetry [Figure 1e (right panel)]. Further, Figure 1f (left and right panels) displays the  $\text{Co}(\text{Ge}_{0.5}\text{Te}_{0.5})_{2.8}\text{Sb}_{0.20}$  sample lattice, characterized by an  $Im\bar{3}$  space group and a  $d$ -spacing of

$0.62 \pm 0.02$  nm assigned to the  $(110)$  plane. Notably, the TEM and electron diffraction patterns were fully consistent with the XRD data.

### 3.2. Band Structure Calculations

In order to evaluate the possible structures of the  $\text{Co}(\text{Ge}_{0.5}\text{Te}_{0.5})_{3-x}\text{Sb}_x$  skutterudites, we first determined which type of atoms would be substituted by Sb (with  $x = 0.0417$ ) by calculating the corresponding formation energies. Because  $\text{Co}(\text{Ge}_{0.5}\text{Te}_{0.5})_3$  has a  $R\bar{3}$  symmetry (space

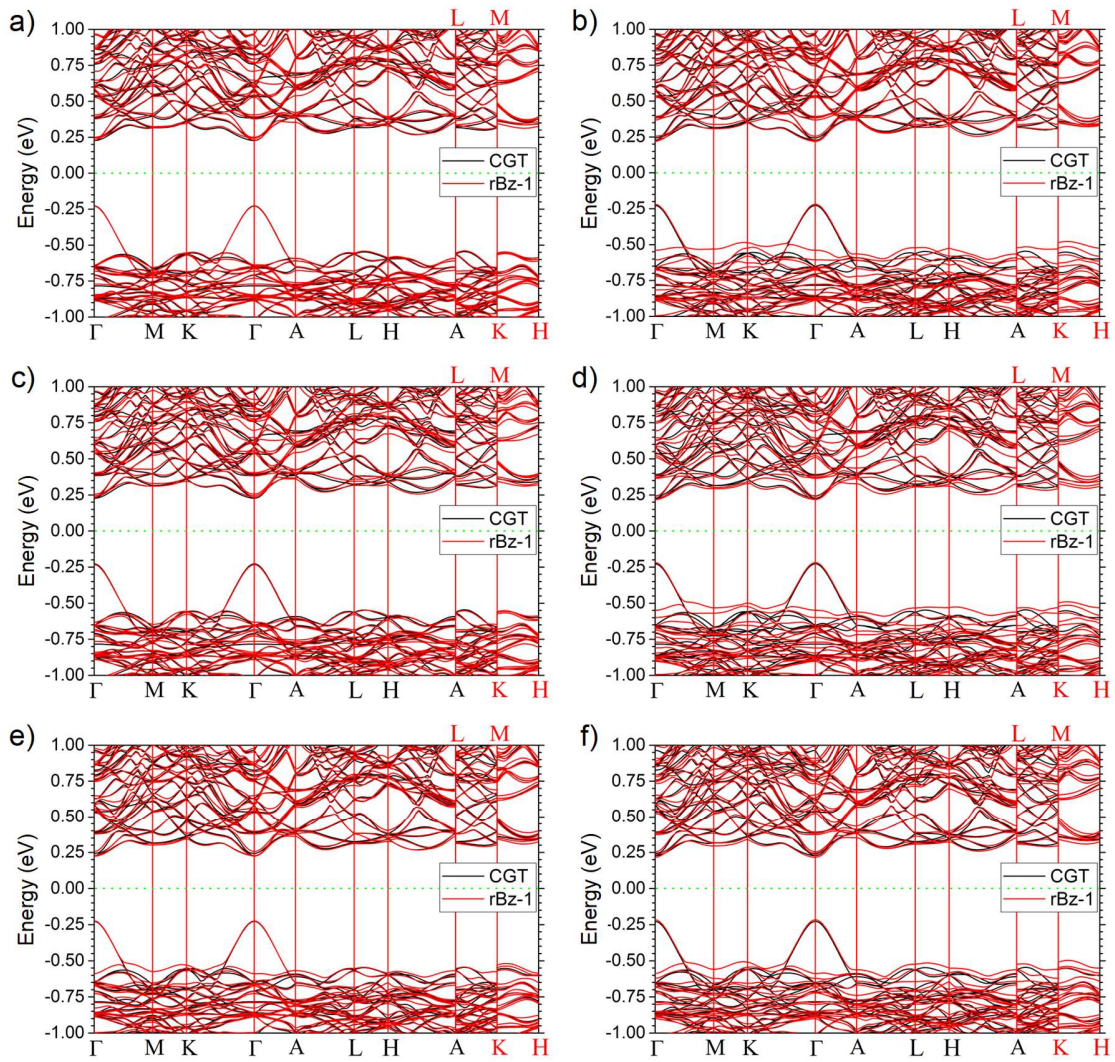


**Figure 2.** Band structures for  $\text{Co}(\text{Ge}_{0.5}\text{Te}_{0.5})_{3-x}\text{Sb}_x$  with  $x = 0.0417$ ,  $0.083$ , and  $0.167$ ; CGT indicates the  $x = 0$  composition, whereas rBz-1 denotes one of the three symmetry related reduced Brillouin zone for Sb-doped structures. The zero of the energy is set halfway between the highest valence band and the lowest conduction band (288<sup>th</sup> and 289<sup>th</sup> bands, respectively) at the  $\Gamma$  point. (a, b) BS for configuration with one Ge(1) or one Te(1) substituted by Sb; (c) BS for configuration with one Ge(1) and one Ge(2) substituted by Sb; (d, e) BS for configurations with Sb substituting one Ge(1) and one Te(1); (f) BS for configuration with two GeTe pairs substituted by two  $\text{Sb}_2$  pairs.

group 148), only six inequivalent positions can be substituted by Sb atoms, and the corresponding formation energies are shown in Table 1. Based on these values, we can conclude that only Ge or Te atoms can be substituted by Sb atoms, because the Co substitution by Sb atoms involves a formation energy approximately 2.5–3 eV higher. Moreover, as the Sb substitution formation energies of the Ge atoms are approximately 0.27 eV lower than those of Te atoms, Ge atoms will likely be substituted by Sb atoms. The Sb-doped  $\text{Co}(\text{Ge}_{0.5}\text{Te}_{0.5})_3$  was predicted to be an *n*-type material, because Sb atoms have one more electron than Ge atoms.

**Table 1:** Formation energies ( $E_{\text{form}}$ ) for single Sb atom substitution.

| Atom\Co-ordinate | x     | y     | z     | Symmetry | $E_{\text{form}}$ (eV) |
|------------------|-------|-------|-------|----------|------------------------|
| Co(1)            | 0.000 | 0.000 | 0.745 | 6c       | 3.399                  |
| Co(2)            | 0.668 | 0.833 | 0.081 | 18f      | 3.288                  |
| Ge(1)            | 0.169 | 0.660 | 0.327 | 18f      | 0.467                  |
| Ge(2)            | 0.398 | 0.284 | 0.283 | 18f      | 0.466                  |
| Te(1)            | 0.613 | 0.732 | 0.232 | 18f      | 0.747                  |
| Te(2)            | 0.488 | 0.172 | 0.168 | 18f      | 0.738                  |

We then considered doping with two Sb atoms (with  $x = 0.083$ ) and four Sb atoms ( $x = 0.167$ ) inside the unit cell, and the corresponding formation energies are plotted in Figure S4. For doping two Sb atoms, according to the crystal symmetry ( $R\bar{3}$ ), Ge and Te atoms are located at Wyckoff positions of 18f (see Table I), once we fix first Sb doping position, we then have 18 (17) possibilities to select the second position of Sb atom with different (same) Wyckoff position. We consider all the doping structures to perform the calculation and found the formation energies could be classified into four categories: (i) formation energies ranging from 0.95 to 1.00 eV when two Ge atoms were substituted by Sb; (ii) formation energies falling into two ranges, 1.23–1.31 and 1.47–1.51 eV, for Sb substitution of two Te atoms; (iii) formation energies in the 0.52–0.57 eV range when two separated Ge and Te atoms were substituted by Sb; and (iv) formation energies ranging from 0.36 to 0.37 eV when a pair of neighboring Ge–Te atoms was substituted by a Sb pair. It is worth noting that the most stable structures for doping with two Sb atoms ( $x = 0.083$ ) were those with a pair of neighboring Ge–Te atoms substituted by two Sb atoms. Overall, the structural configurations with one Ge and one Te substituted by two Sb atoms showed the lowest formation energy, followed by configurations with two Ge atoms substituted by Sb, and finally structures with two Te atoms substituted by two Sb atoms (Figure S4). The Sb substitution for one Ge and one Te atom did not have any doping effect, because the substituted atoms have the same number of valence electrons as

the two doped Sb atoms; therefore, the overall doping effect depends on the difference of the Sb substituted Ge and Te atoms rather than the total number of Sb atoms introduced. This fact complicates the analysis of the experimental data in the skutterudite  $\text{Co}(\text{Ge}_{0.5}\text{Te}_{0.5})_{3-x}\text{Sb}_x$  system, because it is difficult to experimentally control the Sb-substituted Ge and Te atoms. Upon doping with four Sb atoms ( $x = 0.167$ ), we mainly consider some lowest energy doping structures of categories (iv) with neighboring Ge–Te pairs substituted by  $\text{Sb}_2$  pairs. The most stable structures were those with two bonded Ge–Te pairs substituted by two  $\text{Sb}_2$  pairs, with formation energies ranging from 0.71 to 0.76 eV, which are approximately twice the formation energies (0.36–0.37 eV) obtained for structures with one bonded Ge–Te pair substituted by one  $\text{Sb}_2$  pair (Figure S4). This indicates that the pnictogen ring of  $\text{GeTeSb}_2$  would become one of the building blocks for skutterudite  $\text{Co}(\text{Ge}_{0.5}\text{Te}_{0.5})_{3-x}\text{Sb}_x$ . However, we compared the formation energies for all the configurations discussed above, except for the one with two Te atoms substituted by two Sb atoms, and all formation energies were within the 0.35–1.00 eV range; therefore, all configurations should be considered in order to interpret the experimental data. The fundamental question that needs to be addressed is thus whether the band structure of  $\text{Co}(\text{Ge}_{0.5}\text{Te}_{0.5})_{3-x}\text{Sb}_x$  is considerably different from that of  $\text{Co}(\text{Ge}_{0.5}\text{Te}_{0.5})_3$ . To answer this question, we calculated the electronic band structure for different configurations, as shown in Figure 2. The band structures for all Sb-doped  $\text{Co}(\text{Ge}_{0.5}\text{Te}_{0.5})_3$  compositions were almost unchanged or only slightly different compared to that of  $\text{Co}(\text{Ge}_{0.5}\text{Te}_{0.5})_3$ , and the three broken-symmetry band structures related to the reduced Brillouin zone (rBz-1, rBz-2, and rBz-3), due to Sb doping, were very similar to each other (Figure S5). These findings simplified and, more importantly, justified the use of the rigid band approximation<sup>49</sup> to predict, explain, and compare the theoretical results with the experimental measurements reported in the latter section.

### 3.3. Thermoelectric Properties

#### 3.3.1. Electronic Transport

The temperature dependence of the electrical conductivity of the  $\text{Co}(\text{Ge}_{0.5}\text{Te}_{0.5})_{3-x}\text{Sb}_x$  ( $x = 0-0.20$ ) series from room temperature (RT) to 773 K is presented in Figure 3a. The pristine  $\text{Co}(\text{Ge}_{0.5}\text{Te}_{0.5})_3$  sample showed a semiconductor-like behavior, consistent with the report by Kaltzoglou et al.,<sup>26</sup> with the electrical conductivity increasing with increasing temperature. The influence of the Sb incorporation in the ternary  $\text{Co}(\text{Ge}_{0.5}\text{Te}_{0.5})_3$  skutterudite was reflected not only in the temperature dependence, but also the absolute value of  $\sigma$ . Nevertheless, a more complex scenario emerged as we further analyzed the carrier concentration  $n$  and mobility  $\mu_e$ . The room temperature value of  $n$  increased from  $9.7 \times 10^{17}$  to  $4.2 \times 10^{20} \text{ cm}^{-3}$  as  $x$  increased from 0 to 0.20. In theory, donating one electron into the

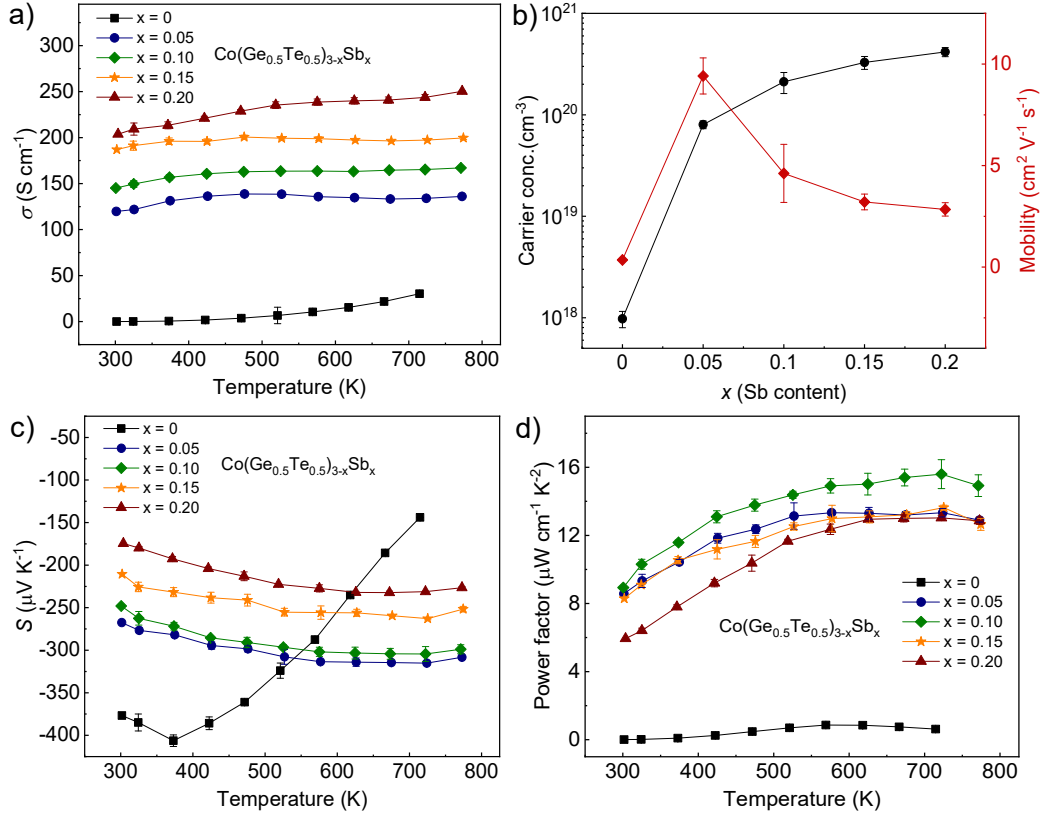


**Figure 3.** Temperature dependences of (a) electrical conductivity, (b) carrier concentration and mobility at RT, (c) Seebeck coefficient, and (d) power factor for the  $\text{Co}(\text{Ge}_{0.5}\text{Te}_{0.5})_{3-x}\text{Sb}_x$  ( $x = 0-0.20$ ) series.

$\text{Co}(\text{Ge}_{0.5}\text{Te}_{0.5})_3$  hexagonal unit cell ( $x = 0.0417$ ) should generate an electron concentration of  $5.039 \times 10^{20} \text{ cm}^{-3}$ ; this would indicate the presence of 0.834 electrons doped in the system at  $x = 0.20$ . Because the Sb doping led to  $n$  rising from  $9.7 \times 10^{17}$  to  $4.2 \times 10^{20} \text{ cm}^{-3}$  as  $x$  increased from 0 to 0.20, the electrical conductivity would be expected to increase by one or two orders of magnitude, as seen in Figure 3a. On the other hand, the corresponding carrier mobility  $\mu_e$  showed a local maximum at  $x = 0.05$  and then decreased in higher Sb-substituted samples. The carrier mobility could be hindered by the appearance of a GeTe phase, as observed in the  $x = 0.10, 0.15$ , and  $0.20$  samples. Compared to the binary skutterudites, all samples showed a much lower carrier mobility, which could be attributed to the large electronegativity difference of the constituent elements. In such materials, atom-to-atom charge fluctuations are known to increase the charge carrier scattering and thereby reduce the carrier mobility.<sup>7</sup>

The temperature dependence of the Seebeck coefficient for the  $\text{Co}(\text{Ge}_{0.5}\text{Te}_{0.5})_{3-x}\text{Sb}_x$  series is shown in Figure 3c. From RT to 773 K, the Seebeck coefficient was negative for all compounds, indicating that electrons were the major carriers. The pristine  $\text{Co}(\text{Ge}_{0.5}\text{Te}_{0.5})_3$  sample ( $x = 0$ ) had a

much higher Seebeck coefficient magnitude at room temperature, and became an intrinsic semiconductor above 373 K. Such mixed conduction behavior in ternary skutterudites has been previously attributed to the substantially different effective masses of the conduction and valence band edges.<sup>31</sup> However, for all Sb-containing compounds, the absolute value of the Seebeck coefficient increased monotonically with the temperature up to 723 K. On the other hand, the magnitude of the Seebeck coefficient decreased with increasing Sb content, due to the increase in carrier concentration. The power factor was calculated by multiplying the squared Seebeck coefficient by the electrical conductivity (Figure 3d). The maximum power factor obtained for pristine  $\text{Co}(\text{Ge}_{0.5}\text{Te}_{0.5})_3$  was  $0.7 \mu\text{W cm}^{-1} \text{K}^{-2}$  at 573 K. Adding Sb resulted in a substantial increased power factor, and the maximum value of  $15.6 \mu\text{W cm}^{-1} \text{K}^{-2}$  was found for the  $x = 0.10$  sample at 723 K.

In order to investigate the electrical properties in relation to the complex electronic band structure, a Pisarenko plot (Figure 4a) was drawn using the doping-dependent Seebeck coefficients at room temperature. In typical degenerate semiconductors, the relationship between  $S$ ,  $m_s^*$ , and  $n$  can be expressed as:

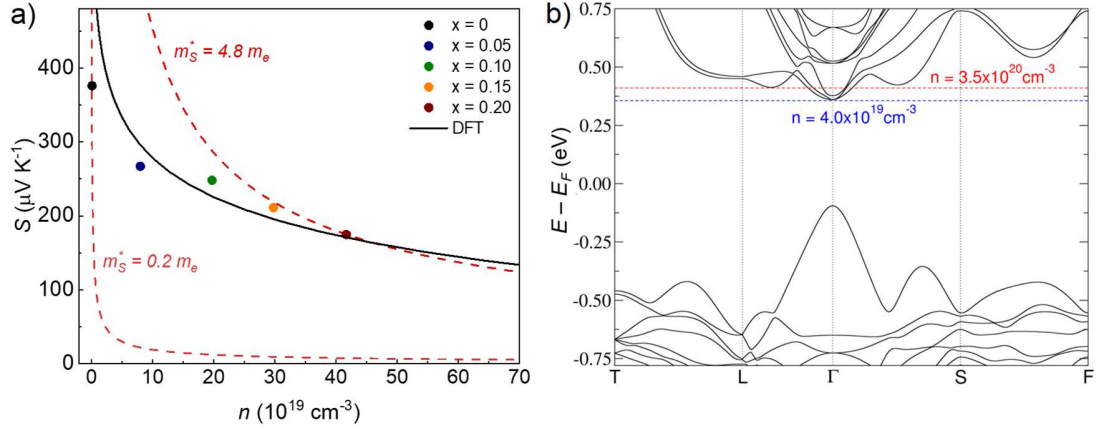


**Figure 4.** (a) Pisarenko plot of measured Seebeck coefficient vs. carrier concentration for the  $\text{Co}(\text{Ge}_{0.5}\text{Te}_{0.5})_{3-x}\text{Sb}_x$  compounds. The solid black line represents the DFT-calculated Seebeck coefficient of pristine  $\text{Co}(\text{Ge}_{0.5}\text{Te}_{0.5})_3$  at 300 K. (b) DFT-calculated band structure for  $\text{Co}(\text{Ge}_{0.5}\text{Te}_{0.5})_3$ . The blue and red dotted lines indicate the electron doping levels corresponding to carrier concentrations of  $4.0 \times 10^{19}$  and  $3.5 \times 10^{20} \text{ cm}^{-3}$ , respectively.

$$S = \frac{2k_B T}{3e\hbar^2} \left(\frac{\pi}{3n}\right)^{\frac{2}{3}} m_S^* (1+r), \quad (1)$$

where  $k_B$  is the Boltzmann constant,  $e$  is the electron charge,  $\hbar$  is the reduced Planck constant,  $r$  is the scattering parameter ( $r = 0$  for acoustic phonon scattering), and  $m_S^*$  is the effective mass obtained from Seebeck measurements according to the single parabolic band (SPB) model.

The pristine  $\text{Co}(\text{Ge}_{0.5}\text{Te}_{0.5})_3$  exhibited a low carrier concentration of  $\sim 1 \times 10^{18} \text{ cm}^{-3}$ . Based on the Seebeck measurements and the SPB model in Equation (1), the pristine  $\text{Co}(\text{Ge}_{0.5}\text{Te}_{0.5})_3$  showed a light-mass behavior ( $\sim 0.2 m_e$ ). Both the carrier concentration and effective mass increased with the Sb content in  $\text{Co}(\text{Ge}_{0.5}\text{Te}_{0.5})_3$ ;  $m_S^*$  was equal to  $4.8 m_e$  for the  $x = 0.2$  sample, clearly showing that at higher carrier concentrations the heavy band dominated the electrical transport (as shown in Figure 4a). The electron transport properties of a material strongly depend on its electronic structure.

As discussed in section 3.2, the overall shape of the band structures of the Sb-doped materials were similar (especially in the conduction band region) to that of pristine  $\text{Co}(\text{Ge}_{0.5}\text{Te}_{0.5})_3$ . Therefore, a theoretical analysis using the rigid band approximation is expected to be accurate. Based on the density functional theory (DFT)-calculated band structures, when the Sb content  $x$  increased from 0 to 0.083 and 0.167, the effective mass of the CBM increased from  $0.42 m_e$  to  $0.57 m_e$  and  $1.33 m_e$ , respectively. Similar trends were also observed in n-type  $\text{CoSb}_3$  (Yb-filled  $\text{CoSb}_3$ ).<sup>9, 10</sup> Moreover, the second conduction band (SCB) is essential for electrical transport in n-type  $\text{CoSb}_3$ , and at high temperature the transport occurs in both bands, resulting in exceptional thermoelectric performances.<sup>10</sup> For  $\text{Co}(\text{Ge}_{0.5}\text{Te}_{0.5})_3$  with heavy electron doping ( $n = 3.5 \times 10^{20}$

$\text{cm}^{-3}$ ), the Fermi level moved up to the SCB, which was located approximately 0.063 eV above the CBM along the  $\Gamma - L$  direction (Figure 4b). The SCB-CB $_{\Gamma}$  gap observed for  $\text{Co}(\text{Ge}_{0.5}\text{Te}_{0.5})_3$  was smaller than that calculated for  $\text{CoSb}_3$  (0.089 eV).<sup>10</sup> Furthermore, the Seebeck coefficients (solid black line in Figure 4a) were calculated based on the pristine  $\text{Co}(\text{Ge}_{0.5}\text{Te}_{0.5})_3$  electronic structures, using the BoltzTraP code with the rigid-band model.<sup>49</sup> The Seebeck coefficients decreased from 316 to 165  $\mu\text{V K}^{-1}$  as the carrier concentration increased from  $6 \times 10^{19}$  to  $4 \times 10^{20} \text{ cm}^{-3}$ . As shown in Figure 4a, the trends of the calculated effective mass and Seebeck coefficients are consistent with the experimental values.

### 3.3.2. Thermal Transport

The experimentally measured total thermal conductivity ( $\kappa$ ) values of the ternary skutterudite  $\text{Co}(\text{Ge}_{0.5}\text{Te}_{0.5})_{3-x}\text{Sb}_x$  samples (Figure 5a) showed a decreasing temperature dependence for all compositions. For comparison, the experimental thermal conductivity of  $\text{CoSb}_3$  is also shown in Figure 5a, and its values are consistent with previous reports.<sup>50</sup> Compared to  $\text{CoSb}_3$ , all  $\text{Co}(\text{Ge}_{0.5}\text{Te}_{0.5})_3$  samples showed a dramatic decrease in thermal conductivity, attributed to the disrupted pnictogen ring with  $\text{Ge}_2\text{Te}_2$  structure. At room temperature, the ( $\kappa$ ) values decreased from  $\sim 9 \text{ W m}^{-1} \text{ K}^{-1}$  for  $\text{CoSb}_3$  to  $\sim 3 \text{ W m}^{-1} \text{ K}^{-1}$  for  $\text{Co}(\text{Ge}_{0.5}\text{Te}_{0.5})_3$ . The lattice thermal conductivities ( $\kappa_L$ ) of the  $\text{Co}(\text{Ge}_{0.5}\text{Te}_{0.5})_{3-x}\text{Sb}_x$  samples (Figure 5b) ranged from 3.2 to 3  $\text{W m}^{-1} \text{ K}^{-1}$  at 300 K, and decreased with increasing temperature. The  $\kappa_L$  value of  $\text{Co}(\text{Ge}_{0.5}\text{Te}_{0.5})_3$  reached a minimum of 1.88  $\text{W m}^{-1} \text{ K}^{-1}$  at 673 K. After doping with Sb,  $\kappa_L$  further decreased to 1.5  $\text{W m}^{-1} \text{ K}^{-1}$  at 723 K for the  $\text{Co}(\text{Ge}_{0.5}\text{Te}_{0.5})_{2.9}\text{Sb}_{0.10}$  sample.

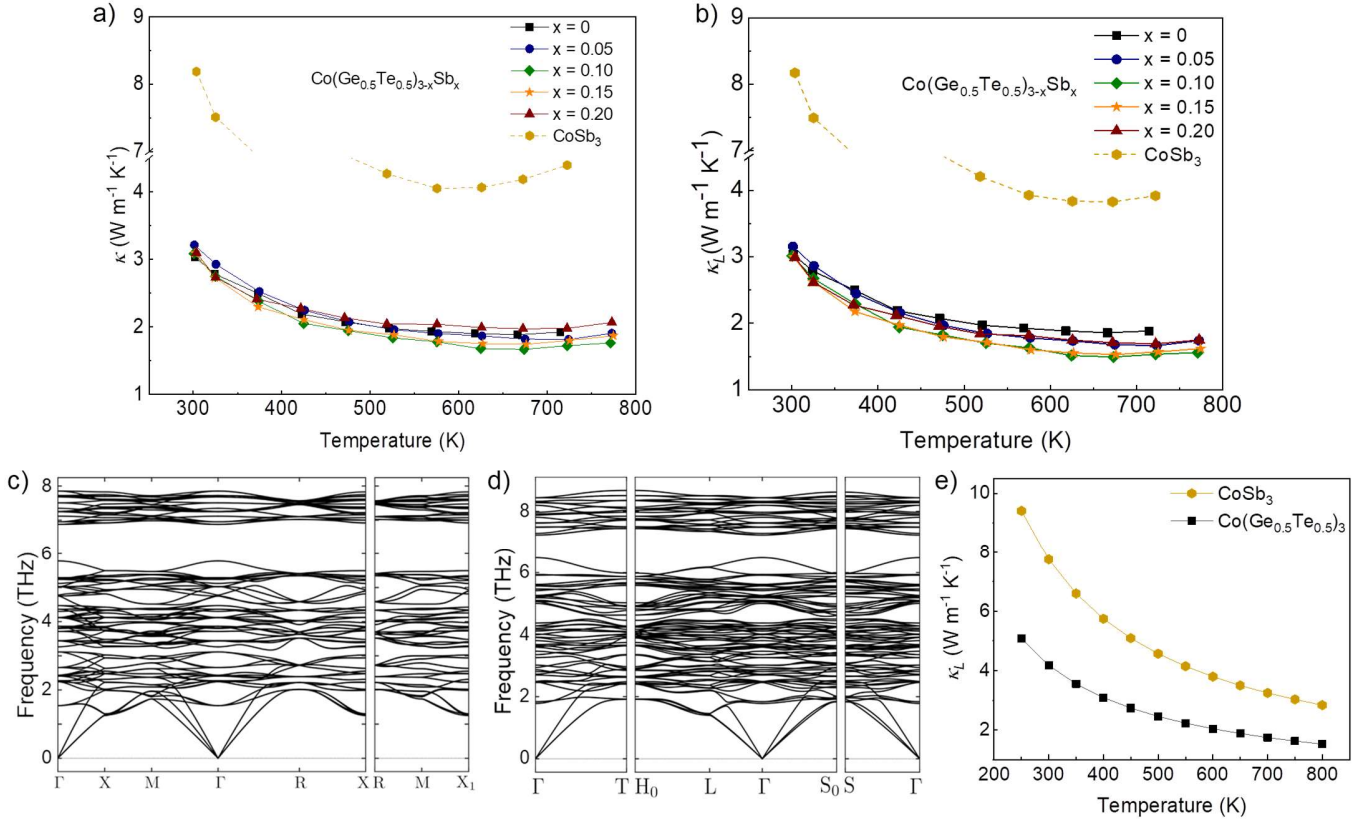


**Figure 5.** (a) Total thermal conductivity of  $\text{Co}(\text{Ge}_{0.5}\text{Te}_{0.5})_{3-x}\text{Sb}_x$  compounds; for comparison, the values of  $\text{CoSb}_3$  are also shown. (b) Lattice contributions to thermal conductivity ( $\kappa_L$ ) for  $\text{Co}(\text{Ge}_{0.5}\text{Te}_{0.5})_3$  and  $\text{CoSb}_3$ . (c, d) Calculated phonon dispersion curves for (c)  $\text{CoSb}_3$  and (d)  $\text{Co}(\text{Ge}_{0.5}\text{Te}_{0.5})_3$ . (e) Calculated lattice thermal conductivities for  $\text{CoSb}_3$  and  $\text{Co}(\text{Ge}_{0.5}\text{Te}_{0.5})_3$ .

Because the lattice contribution dominates the thermal conductivity of both  $\text{CoSb}_3$  and  $\text{Co}(\text{Ge}_{0.5}\text{Te}_{0.5})_3$ , as shown in Figure 5b, we performed first-principles phonon calculations to study the lattice dynamics and understand the origin of the dramatic reduction in thermal conductivity upon twisting the anion ring. This analysis can reveal the actual mechanism for the reduction of  $\kappa_L$  after disrupting the anion rings in the skutterudite structure. The calculated phonon dispersion spectra of  $\text{CoSb}_3$  and  $\text{Co}(\text{Ge}_{0.5}\text{Te}_{0.5})_3$  (Figures 5c and 5d, respectively) are consistent with previous theoretical studies.<sup>34, 51</sup> The corresponding calculated  $\kappa_L$  values are shown in Figure 5e. These theoretical values are in good agreement with the experimental data, with slight differences likely due to additional scattering by nanoscale grains and impurities. Moreover, the Raman modes of the  $\text{Co}(\text{Ge}_{0.5}\text{Te}_{0.5})_3$  samples, as calculated from the phonon spectra, are consistent with the experimental Raman measurements (Figure S6). To obtain further insight into the mechanism behind the different phonon thermal transport in  $\text{CoSb}_3$  and

$\text{Co}(\text{Ge}_{0.5}\text{Te}_{0.5})_3$ , we conducted a detailed analysis of their phonon-related properties.

In the single-mode relaxation time approximation (RTA) solution to the Boltzmann transport equation, the lattice thermal conductivity tensor can be written in closed form as follows:<sup>46</sup>

$$\kappa_L = \frac{1}{NV_0} \sum_{\lambda} C_{\lambda} v_{\lambda} \otimes v_{\lambda} \tau_{\lambda}^{SMRT} \quad (2)$$

where  $V_0$  is the volume of a unit cell,  $C_{\lambda}$  is the mode-dependent heat capacity, and  $v_{\lambda}$  and  $\tau_{\lambda}^{SMRT}$  are the group velocity and phonon lifetime of phonon mode  $\lambda$ , respectively. This indicates that any change in the mode heat capacity, group velocity, or phonon lifetime has a significant effect on  $\kappa_L$ . The  $C_{\lambda}$  and  $v_{\lambda}$  parameters can be calculated within the harmonic approximation. Owing to their similar crystal structure and number of atoms, the two samples showed similar phonon dispersion curves with minor differences; for instance, the first optical mode at the  $\Gamma$  point of  $\text{Co}(\text{Ge}_{0.5}\text{Te}_{0.5})_3$  was lower than that of  $\text{CoSb}_3$ , due to the atomic mass difference between Ge, Te, and Sb atoms.

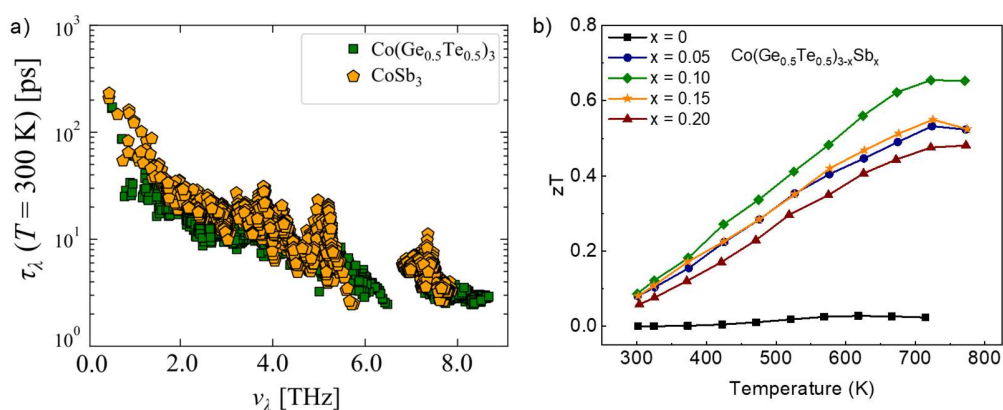


**Fig. 6** (a) Calculated phonon lifetimes for CoSb<sub>3</sub> and Co( $\text{Ge}_{0.5}\text{Te}_{0.5}$ )<sub>3</sub>. (b) Temperature dependence of  $zT$  for Co( $\text{Ge}_{0.5}\text{Te}_{0.5}$ )<sub>3-x</sub>Sb<sub>x</sub>.

These minor differences were reflected in the similar magnitudes of the calculated heat capacity and phonon group velocities, as shown in Figure S7. This indicates that the slight increase in the  $C_\lambda$  and  $v_\lambda$  values is insufficient to explain the observed decrease in  $\kappa_L$ ; thus, the phonon lifetime, as the only quantity left in Equation (2), must be significantly reduced in the anion-disrupted ternary skutterudites.

The frequency-dependent phonon lifetimes of the acoustic and optical phonon modes at room temperature for both CoSb<sub>3</sub> and Co( $\text{Ge}_{0.5}\text{Te}_{0.5}$ )<sub>3</sub> are presented in Figure 6a. The comparison highlights an evident reduction in the phonon lifetimes for the ternary skutterudites, confirming that the increased scattering rate ( $\tau_\lambda^{-1}$ ) was the main reason for the observed reduction in  $\kappa_L$ . In addition, the increased scattering rate was only observed for the low-frequency (up to 3 THz) phonon spectrum. At room temperature, the low-frequency (up to 3 THz) phonons associated with the pnictogen ring vibrations represent the main contribution to the  $\kappa_L$  of CoSb<sub>3</sub>.<sup>51</sup> This clearly indicates that the vibrational modes associated with the twisted  $\text{Ge}_2\text{Te}_2$  rings caused significant scattering of the low-frequency phonons and inhibited heat transport in the ternary skutterudites. The temperature dependence of the  $zT$  values of the Co( $\text{Ge}_{0.5}\text{Te}_{0.5}$ )<sub>3-x</sub>Sb<sub>x</sub> series is shown in Figure 6b. The combination of enhanced power factor and moderately low thermal conductivity resulted in a maximum  $zT$ , which increased from  $\sim 0.02$  for Co( $\text{Ge}_{0.5}\text{Te}_{0.5}$ )<sub>3</sub> to 0.65 for Co( $\text{Ge}_{0.5}\text{Te}_{0.5}$ )<sub>2.9</sub>Sb<sub>0.10</sub> at 723 K.

#### 4. CONCLUSIONS

In this study, we reported for the first time the thermoelectric properties of ternary Co( $\text{Ge}_{0.5}\text{Te}_{0.5}$ )<sub>3-x</sub>Sb<sub>x</sub>, including ordered ( $0 \leq x \leq 0.05$ ) and ideal ( $0.10 \leq x \leq 0.20$ ) skutterudite structures. A rhombohedral to cubic phase

transition was found to occur upon Sb substitution. Based on DFT results and experimental data, we showed that incorporating antimony into Co( $\text{Ge}_{0.5}\text{Te}_{0.5}$ )<sub>3</sub> favored the substitution of Ge rather than Te atoms and introduced electrons in the system. In addition, we demonstrated that, for heavily doped compositions, a secondary conduction band contributed to the carrier transport along with the primary band. The band structure of Co( $\text{Ge}_{0.5}\text{Te}_{0.5}$ )<sub>3</sub> was not altered upon Sb doping up to  $x = 0.167$ , which justified the use of rigid band approximation to calculate doping dependent thermopower and effective mass, which were in agreement with experimental data. The moderately high thermopower along with enhanced electrical conductivity resulted in an improved thermoelectric power factor. Furthermore, we studied the lattice dynamics of binary (CoSb<sub>3</sub>) and mixed-anion [Co( $\text{Ge}_{0.5}\text{Te}_{0.5}$ )<sub>3</sub>] skutterudites by solving the linearized Boltzmann equation based on first-principles anharmonic calculations. The reduction in lattice thermal conductivity of mixed-anion skutterudites was largely due to increased scattering of low-frequency phonons. The incorporation of Sb in Co( $\text{Ge}_{0.5}\text{Te}_{0.5}$ )<sub>3</sub> ultimately led to a 30-fold increase in the thermoelectric figure-of-merit.

#### ASSOCIATED CONTENT

**Supporting Information:** This material is available free of charge via the Internet at <http://pubs.acs.org>.

#### AUTHOR INFORMATION

##### Corresponding Author

**Kuei-Hsien Chen** — Institute of Atomic and Molecular Sciences, Academia Sinica, Taipei 10617, Taiwan; Center for Condensed Matter Sciences, National Taiwan University, Taipei 10617, Taiwan; Email: [chenkh@pubs.iams.sinica.edu.tw](mailto:chenkh@pubs.iams.sinica.edu.tw)

**Li-Chyong Chen** — Center for Condensed Matter Sciences, National Taiwan University, Taipei 10617, Taiwan; Center of Atomic Initiative for New Materials, National Taiwan University, Taipei 10617, Taiwan; Email: chenlc@ntu.edu.tw

**Ching-Ming Wei** — Institute of Atomic and Molecular Sciences, Academia Sinica, Taipei 10617, Taiwan; Email: cmw@phys.sinica.edu.tw

#### Authors

**Suneesh Meledath Valiyaveetil** — Institute of Atomic and Molecular Sciences, Academia Sinica, Taipei 10617, Taiwan; Department of Physics, National Central University, Taoyuan 32001, Taiwan; Molecular Science and Technology Program, Taiwan International Graduate Program, Academia Sinica, Taipei 11529, Taiwan; Center for Condensed Matter Sciences, National Taiwan University, Taipei 10617, Taiwan

**Duc-Long Nguyen** — Institute of Atomic and Molecular Sciences, Academia Sinica, Taipei 10617, Taiwan

**Deniz P. Wong** — Institute of Atomic and Molecular Sciences, Academia Sinica, Taipei 10617, Taiwan; Helmholtz-Zentrum Berlin für Materialien und Energie, Albert-Einstein-Straße 15, 12489 Berlin, Germany

**Cheng-Rong Hsing** — Institute of Atomic and Molecular Sciences, Academia Sinica, Taipei 10617, Taiwan

**Laura Paradis-Fortin** — Institute of Atomic and Molecular Sciences, Academia Sinica, Taipei 10617, Taiwan

**Mohammad Qorbani** — Center for Condensed Matter Sciences, National Taiwan University, Taipei 10617, Taiwan; Center of Atomic Initiative for New Materials, National Taiwan University, Taipei 10617, Taiwan

**Amr Sabbah** — Institute of Atomic and Molecular Sciences, Academia Sinica, Taipei 10617, Taiwan; Tabbin Institute for Metallurgical Studies, Tabbin, Helwan 109, Cairo 11421, Egypt

**Ta-Lei Chou** — Institute of Atomic and Molecular Sciences, Academia Sinica, Taipei 10617, Taiwan

**Kuei-Kuan Wu** — Institute of Atomic and Molecular Sciences, Academia Sinica, Taipei 10617, Taiwan

**Vasudevan Rathinam** — Institute of Atomic and Molecular Sciences, Academia Sinica, Taipei 10617, Taiwan

#### Author Contributions

SMV: conceptualization, writing – original draft, formal analysis, investigation, and visualization. DLN, CRH and CMW: software, formal analysis, validation. DPW and LPF: formal analysis, validation, and writing – review & editing. MQ and AS: formal analysis and validation. TLC, KKW and RV: methodology, LCC and KHC: supervision, validation, funding acquisition, writing – review & editing.

#### Notes

The authors declare no competing financial interest.

#### ACKNOWLEDGMENT

This work was supported by the Center for Sustainability Science, Academia Sinica under project AS-SS-109-0110 and the Center of Atomic Initiative for New Materials (AI-Mat), National Taiwan University (109L9008), funded by the Featured Areas Research Center Program with-in the framework of the Higher Education Sprout Project by the Ministry of Education (MOE) of Taiwan. C.M.W. and C.R.H. acknowledge support from Academia Sinica under project AS-SS-109-01-40 and C.M.W. and D.L.N. acknowledge support from the Ministry of Science and Technology of Taiwan under Grant No. MOST 108-2112-M-001-043-MY3. The authors are grateful to Dr. Yu-Chun Chuang for the assistance on the high-resolution XRD at TPS 19A in the National Synchrotron Radiation Research Center (NSRRC, Taiwan).

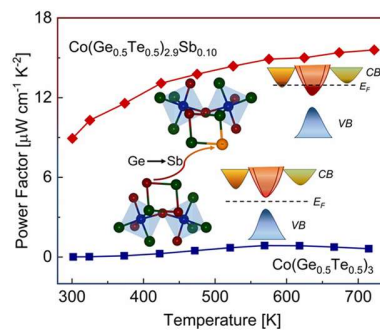
#### REFERENCES

1. DiSalvo, F. J., Thermoelectric cooling and power generation. *Science* **1999**, *285* (5428), 703-6.
2. Snyder, G. J.; Toberer, E. S., Complex thermoelectric materials. *Nat Mater* **2008**, *7* (2), 105-14.
3. Tan, G. J.; Zhao, L. D.; Kanatzidis, M. G., Rationally Designing High-Performance Bulk Thermoelectric Materials. *Chem Rev* **2016**, *116* (19), 12123-12149.
4. Shi, X. L.; Zou, J.; Chen, Z. G., Advanced Thermoelectric Design: From Materials and Structures to Devices. *Chem Rev* **2020**, *120* (15), 7399-7515.
5. Haras, M.; Skotnicki, T., Thermoelectricity for IoT - A review. *Nano Energy* **2018**, *54*, 461-476.
6. Petsagkourakis, I.; Tybrandt, K.; Crispin, X.; Ohkubo, I.; Satoh, N.; Mori, T., Thermoelectric materials and applications for energy harvesting power generation. *Sci Technol Adv Mat* **2018**, *19* (1), 836-862.
7. Slack, G. A., *Handbook of Thermoelectrics*. Chemical Rubber, Boca Raton, FL: 1995.
8. Uher, C., Skutterudites: Prospective novel thermoelectrics. *Recent Trends in Thermoelectric Materials Research I* **2001**, *69*, 139-253.
9. Tang, Y.; Gibbs, Z. M.; Agapito, L. A.; Li, G.; Kim, H.-S.; Nardelli, Marco B.; Curtarolo, S.; Snyder, G. J., Convergence of multi-valley bands as the electronic origin of high thermoelectric performance in CoSb<sub>3</sub> skutterudites. *Nature Materials* **2015**, *14* (12), 1223-1228.
10. Hanus, R.; Guo, X. Y.; Tang, Y. L.; Li, G. D.; Snyder, G. J.; Zeier, W. G., A Chemical Understanding of the Band Convergence in Thermoelectric CoSb<sub>3</sub> Skutterudites: Influence of Electron Population, Local Thermal Expansion, and Bonding Interactions. *Chem. Mater.* **2017**, *29* (3), 1156-1164.
11. Isaacs, E. B.; Wolverton, C., Electronic Structure and Phase Stability of Yb-Filled CoSb<sub>3</sub> Skutterudite Thermoelectrics from First-Principles. *Chem. Mater.* **2019**, *31* (16), 6154-6162.
12. Wang, Z. Y.; Xi, J. Y.; Ning, J. Y.; Guo, K.; Duan, B.; Luo, J.; Snyder, G. J.; Yang, J.; Zhang, W. Q., Temperature-Dependent Band Renormalization in CoSb<sub>3</sub> Skutterudites Due to Sb-Ring-Related Vibrations. *Chem. Mater.* **2021**, *33* (3), 1046-1052.
13. Sales, B. C.; Mandrus, D.; Williams, R. K., Filled Skutterudite Antimonides: A New Class of Thermoelectric Materials. *Science* **1996**, *272* (5266), 1325-8.
14. Gainza, J.; Serrano-Sanchez, F.; Rodrigues, J. E.; Prado-Gonjal, J.; Nemes, N. M.; Biskup, N.; Dura, O. J.; Martinez, J. L.; Fauth, F.; Alonso, J. A., Unveiling the Correlation between the Crystalline Structure of M-Filled CoSb<sub>3</sub>(M = Y, K, Sr) Skutterudites and Their Thermoelectric Transport Properties. *Adv. Funct. Mater.* **2020**, *30* (36).

15. Nolas, G. S.; Kaeser, M.; Littleton, R. T.; Tritt, T. M., High figure of merit in partially filled ytterbium skutterudite materials. *Appl. Phys. Lett.* **2000**, *77* (12), 1855-1857.
16. Nolas, G. S.; Slack, G. A.; Morelli, D. T.; Tritt, T. M.; Ehrlich, A. C., The effect of rare-earth filling on the lattice thermal conductivity of skutterudites. *J. Appl. Phys.* **1996**, *79* (8), 4002-4008.
17. Shi, X.; Yang, J.; Salvador, J. R.; Chi, M.; Cho, J. Y.; Wang, H.; Bai, S.; Yang, J.; Zhang, W.; Chen, L., Multiple-Filled Skutterudites: High Thermoelectric Figure of Merit through Separately Optimizing Electrical and Thermal Transports. *Journal of the American Chemical Society* **2011**, *133* (20), 7837-7846.
18. Toprak, M. S.; Stiewe, C.; Platzek, D.; Williams, S.; Bertini, L.; Muller, E. C.; Gatti, C.; Zhang, Y.; Rowe, M.; Muhammed, M., The impact of nanostructuring on the thermal conductivity of thermoelectric CoSb<sub>3</sub>. *Adv. Funct. Mater.* **2004**, *14* (12), 1189-1196.
19. Rogl, G.; Grytsiv, A.; Yubuta, K.; Puchegger, S.; Bauer, E.; Raju, C.; Mallik, R. C.; Rogl, P., In-doped multifilled n-type skutterudites with ZT=1.8. *Acta Mater.* **2015**, *95*, 201-211.
20. Khan, A. U.; Kobayashi, K.; Tang, D. M.; Yamauchi, Y.; Hasegawa, K.; Mitome, M.; Xue, Y. M.; Jiang, B. Z.; Tsuchiya, K.; Golberg, D.; Bando, Y.; Mori, T., Nano-micro-porous skutterudites with 100% enhancement in ZT for high performance thermoelectricity. *Nano Energy* **2017**, *31*, 152-159.
21. Feldman, J. L.; Singh, D. J., Lattice dynamics of skutterudites: First-principles and model calculations for CoSb<sub>3</sub>. *Phys Rev B Condens Matter* **1996**, *53* (10), 6273-6282.
22. Dimitrov, I. K.; Manley, M. E.; Shapiro, S. M.; Yang, J.; Zhang, W.; Chen, L. D.; Jie, Q.; Ehlers, G.; Podlesnyak, A.; Camacho, J.; Li, Q. A., Einstein modes in the phonon density of states of the single-filled skutterudite Yb<sub>0.2</sub>Co<sub>4</sub>Sb<sub>12</sub>. *Phys Rev B* **2010**, *82* (17).
23. King, R. B., Chemical bonding topology of binary and ternary transition-metal polyphosphides. *Inorg. Chem.* **1989**, *28* (15), 3048-3051.
24. Fleurial, J. P.; Caillat, T.; Borshchevsky, A., Skutterudites: An update. *Proceedings Ict'97 - XVI International Conference on Thermoelectrics* **1997**, 1-11.
25. Bos, J. W. G.; Cava, R. J., Synthesis, crystal structure and thermoelectric properties of IrSn<sub>1.5</sub>Te<sub>1.5</sub>-based skutterudites. *Solid State Commun.* **2007**, *141* (1), 38-41.
26. Kaltzoglou, A.; Powell, A. V.; Knight, K. S.; Vaqueiro, P., High-temperature order-disorder transitions in the skutterudites CoGe<sub>1.5</sub>Q<sub>1.5</sub> (Q=S, Te). *J. Solid State Chem.* **2013**, *198*, 525-531.
27. Vaqueiro, P.; Sobany, G. G.; Powell, A. V.; Knight, K. S., Structure and thermoelectric properties of the ordered skutterudite CoGe<sub>1.5</sub>Te<sub>1.5</sub>. *J. Solid State Chem.* **2006**, *179* (7), 2047-2053.
28. Vaqueiro, P.; Sobany, G. G.; Powell, A. V., A synchrotron powder X-ray diffraction study of the skutterudite-related phases AB<sub>(1.5)</sub>Te<sub>(1.5)</sub> (A = Co, Rh, Ir; B = Ge, Sn). *Dalton T* **2010**, *39* (4), 1020-1026.
29. Jung, D.; Whangbo, M. H.; Alvarez, S., Importance of the X<sub>4</sub> ring orbitals for the semiconducting, metallic, or superconducting properties of skutterudites MX<sub>3</sub> and RM<sub>4</sub>X<sub>12</sub>. *Inorg. Chem.* **1990**, *29* (12), 2252-2255.
30. Zevalkink, A.; Star, K.; Aydemir, U.; Snyder, G. J.; Fleurial, J.-P.; Bux, S.; Vo, T.; von Allmen, P., Electronic structure and thermoelectric properties of pnictogen-substituted ASn<sub>1.5</sub>Te<sub>1.5</sub> (A = Co, Rh, Ir) skutterudites. *J. Appl. Phys.* **2015**, *118* (3).
31. Crawford, C. M.; Ortiz, B. R.; Gorai, P.; Stevanovic, V.; Toberer, E. S., Experimental and computational phase boundary mapping of Co<sub>4</sub>Sn<sub>6</sub>Te<sub>6</sub>. *J Mater Chem A* **2018**, *6* (47), 24175-24185.
32. Bang, S.; Wee, D.; Li, A.; Fornari, M.; Kozinsky, B., Thermoelectric properties of pnictogen-substituted skutterudites with alkaline-earth fillers using first-principles calculations. *J. Appl. Phys.* **2016**, *119* (20).
33. Lin, Q.; Smalley, A. L. E.; Johnson, D. C.; Martin, J.; Nolas, G. S., Synthesis and properties of CexCo<sub>4</sub>Ge<sub>6</sub>Se<sub>6</sub>. *Chem. Mater.* **2007**, *19* (26), 6615-6620.
34. Volja, D.; Kozinsky, B.; Li, A.; Wee, D.; Marzari, N.; Fornari, M., Electronic, vibrational, and transport properties of pnictogen-substituted ternary skutterudites. *Phys Rev B* **2012**, *85* (24).
35. Rodriguezcarvajal, J., Recent Advances in Magnetic-Structure Determination by Neutron Powder Diffraction. *Physica B* **1993**, *192* (1-2), 55-69.
36. Roisnel, T.; Rodriguez-Carvajal, J., WinPLOTR: A Windows tool for powder diffraction pattern analysis. *Epdic 7: European Powder Diffraction, Pts 1 and 2* **2001**, 378-3, 118-123.
37. Finger, L. W.; Cox, D. E.; Jephcoat, A. P., A Correction for Powder Diffraction Peak Asymmetry Due to Axial Divergence. *J. Appl. Crystallogr.* **1994**, *27*, 892-900.
38. Alleno, E.; Berardan, D.; Byl, C.; Candolfi, C.; Daou, R.; Decourt, R.; Guilmeau, E.; Hebert, S.; Hejtmanek, J.; Lenoir, B.; Masschelein, P.; Ohorodnichuk, V.; Pollet, M.; Populoh, S.; Ravot, D.; Rouleau, O.; Soulier, M., Invited article: A round robin test of the uncertainty on the measurement of the thermoelectric dimensionless figure of merit of Co<sub>0.97</sub>Ni<sub>0.03</sub>Sb<sub>3</sub>. *Rev. Sci. Instrum.* **2015**, *86* (1), 011301.
39. Kresse, G.; Furthmuller, J., Efficient iterative schemes for ab initio total-energy calculations using a plane-wave basis set. *Phys Rev B* **1996**, *54* (16), 11169-11186.
40. Kresse, G.; Joubert, D., From ultrasoft pseudopotentials to the projector augmented-wave method. *Phys Rev B* **1999**, *59* (3), 1758-1775.
41. Blochl, P. E., Projector Augmented-Wave Method. *Phys Rev B* **1994**, *50* (24), 17953-17979.
42. J. P. Perdew, P. Z., and H. Eschrig, *Electronic Structure of Solids 91*. Akademie Verlag, Berlin: 1991; Vol. 11.
43. Perdew, J. P.; Burke, K.; Ernzerhof, M., Generalized gradient approximation made simple (vol 77, pg 3865, 1996). *Phys. Rev. Lett.* **1997**, *78* (7), 1396-1396.
44. Eriksson, F.; Fransson, E.; Erhart, P., The Hiphive Package for the Extraction of High-Order Force Constants by Machine Learning. *Adv Theor Simul* **2019**, *2* (5).
45. Togo, A.; Tanaka, I., First principles phonon calculations in materials science. *Scripta Mater.* **2015**, *108*, 1-5.
46. Togo, A.; Chaput, L.; Tanaka, I., Distributions of phonon lifetimes in Brillouin zones. *Phys Rev B* **2015**, *91* (9).
47. Vaqueiro, P.; Sobany, G. G.; Stindl, M., Structure and electrical transport properties of the ordered skutterudites MGe<sub>1.5</sub>Sn<sub>1.5</sub> (M=Co, Rh, Ir). *J. Solid State Chem.* **2008**, *181* (4), 768-776.
48. Partik, M.; Lutz, H. D., Semiempirical band structure calculations on skutterudite-type compounds. *Phys. Chem. Miner.* **1999**, *27* (1), 41-46.
49. Madsen, G. K. H.; Singh, D. J., BoltzTraP. A code for calculating band-structure dependent quantities. *Comput. Phys. Commun.* **2006**, *175* (1), 67-71.
50. Sharp, J. W.; Jones, E. C.; Williams, R. K.; Martin, P. M.; Sales, B. C., Thermoelectric Properties of Cosb<sub>3</sub> and Related Alloys. *J. Appl. Phys.* **1995**, *78* (2), 1013-1018.

51. Guo, R.; Wang, X.; Huang, B., Thermal conductivity of skutterudite  $\text{CoSb}_3$  from first principles: Substitution and nanoengineering effects. *Sci Rep* 2015, 5, 7806.

## Table of Contents



The incorporation of Sb in  $\text{Co}(\text{Ge}_{0.5}\text{Te}_{0.5})_3$  leads to more than a 20 times increase in the thermoelectric performance by band structure engineering. This finding opens the way to new skutterudite materials with tunable electronic properties that are desirable for thermoelectric applications.